Available online at www.sciencedirect.com
ScienceDirect
Trans. Nonferrous Met. Soc. China 25(2015) 1011−1019
Transactions of Nonferrous Metals Society of China
www.tnmsc.cn

Interaction between AE44 magnesium alloy and $SiC-Al_2O_3-SiO_2$ ceramic foam

Matej STEINACHER[1], Primož MRVAR[2], Franc ZUPANIČ[1]

1. Faculty of Mechanical Engineering, University of Maribor, Smetanova ulica 17, SI-2000 Maribor, Slovenia;
2. Faculty of Natural Sciences and Engineering, University of Ljubljana,
Aškerčeva cesta 12, SI-1000 Ljubljana, Slovenia

Received 5 May 2014; accepted 8 October 2014

Abstract: The interaction between a molten magnesium alloy AE44 and a $SiC-Al_2O_3-SiO_2$ ceramics and the resulting reaction products were studied. The samples were investigated using optical and electron microscopy, energy dispersive X-ray spectroscopy and X-ray diffraction. SiO_2 was predominantly reduced by Mg during the contact of the magnesium-rich melt with the ceramics. The main reaction product was MgO, whilst Si dissolved in the melt. Two novel tetragonal phases formed at the interface: AlSiRE and AlMgSiRE, having a specific mutual crystallographic orientation relationship. The interactions resulted in strongly connected interfaces between the metal and ceramics after short interaction time; however, interactions lead to disintegration of the ceramics after longer contact time.

Key words: metal matrix composites; AE44 Mg alloy; ceramics; interfacial reaction

---

1 Introduction

Metal-matrix composites (MMCs) show improved performances over their matrix alloys. Magnesium matrix composites can offer potential applications within the automobile and aircraft industries. Interpenetrating phase composites (IPCs) usually display superior mechanical properties compared to conventional MMCs reinforced with particles, intermetallic phases, ceramics, and carbon fibres. A unique combination of cellular ceramic materials, with high mechanical strengths and stiffness at low fractional densities, and the ductility of the metallic phase may be considered as a major advantage of metal/ceramic IPCs [1]. They can be produced in various ways [2,3]. The infiltration can be achieved by spontaneous infiltration phenomenon [4−6], gas pressure-assisted infiltration [7,8], or squeeze-casting into a cellular ceramic preform [1,9,10]. Interface behaviour between the matrix and the reinforcement can profoundly affect the properties of the MMCs [11]. The reinforcement type, alloying element, solidification condition, and heat-treatment of MMCs can affect the local chemical composition and the extent of the interfacial reactions of the MMCs [12].

ZESCHKY et al [1,9,10] investigated these IPCs, using ceramic foam as a reinforcing phase. The MgO and Mg_2Si interfacial reaction products were present at the interface between AZ91 alloy and oxidized $SiC-SiO_2-C-Si$ ceramic foam, whilst very small amounts of MgO were found in the strut's centres. Also, Mg_2Si, MgO, and $Al_{12}Mg_{17}$ were found in the struts of the ceramic foam (SiO_2) infiltrated with AZ31 alloy. $MgAl_2O_4$, $Mg_2Al_4Si_5O_{18}$, and Mg_2Si were formed at the interface between the AZ31 alloy and $SiO_2-Al_2O_3$ ceramic foam.

The interfacial reactions between the Mg-based alloys and ceramic materials have been studied by several researchers (Table 1). BRASZCZYŃSKA et al [13,14] investigated the Mg−3%RE (mass fraction) alloy reinforced with SiC particles. A thick layer was observed at the interface consisting mainly of fine MgO crystals and Ce_3Si_2 or RE_3Si_2 particles, whilst at the interfaces between the ZE63 alloy and SiC particles, the CeO_2 and ZrO_2 were formed [15]. HACK et al [16,17], PAGE et al [18], and McMINN et al [19] found the MgO particles at interfaces between the ZE41 alloy and the α-Al_2O_3 fibres. HU et al [20] reported the presence of reaction products MgO and Al_2RE within the interface region between the AE44 alloy and the short Al_2O_3 fibres.

This short overview clearly showed that types of the

Corresponding author: Matej STEINACHER; E-mail: matej.steinacher@um.si
DOI: 10.1016/S1003-6326(15)63692-5

Table 1 Interfacial reaction products formed at interface between Mg-based alloys and different types of reinforcements

Matrix/reinforcement interface	Reaction product
AZ91/SiC−SiO_2−C−Si ceramic foam	MgO, Mg_2Si [1]
AZ31/SiO_2 ceramic foam	MgO, Mg_2Si [9]
AZ31/SiO_2−Al_2O_3 ceramic foam	$MgAl_2O_4$, $Mg_2Al_4Si_5O_{18}$, Si, Mg_2Si [10]
Pure Mg/SiC particles	MgO, Mg_2Si [21]
Mg−RE3/SiC particles	MgO, Ce_3Si_2 or RE_3Si_2 [13,14]
ZE63/SiC particles	CeO_2, ZrO_2 [15]
AZ91/SiC particles	MgO, Mg_2Si, Al_4C_3 [22] and MgO, $MgAl_2O_4$, AlN [23]
AZ91/SiC whiskers	MgO [24]
AZ91/SiC nano-particles	Mg_2Si [25,26]
Pure Mg/Al_2O_3 fibres	MgO [16,18], Mg_2Si [27], and $MgAl_2O_4$ [28]
ZE41/Al_2O_3 fibres	MgO [16−19]
AE44/Al_2O_3 short-fibres	MgO, Al_2RE [20]
AS21/Al_2O_3 fibres	MgO [29]
AZ91/Al_2O_3 fibres	MgO [30,31]

reaction products strongly depend on the system's metal−ceramics and the processing conditions. In this work, we used a ceramic preform consisting of SiC, Al_2O_3, and SiO_2 that can be produced in different shapes using a simple and low-cost procedure, and the magnesium alloy AE44 containing 4% Al and 4% RE (mischmetal), which is characterized by good ductility and strength. This metal/ceramics composite has never been investigated as yet. It is to be expected that interfacial reactions can profoundly affect the properties of the resulting composite. Thus, in this work, the main focus was given to the characterization of the metal/ceramic interface, and the determination of the reaction products.

2 Experimental

As mentioned previously, an AE44 magnesium alloy and SiC−Al_2O_3−SiO_2 ceramics were used for investigating the metal−ceramic interactions. The composition of the investigated AE44 alloy was determined using ICP-AES (Table 2). The content of Al was around 5%, and the total content of the rare-earth elements was around 4%. The composition of the ceramics was determined using XRF (Table 3). The ceramic samples used during the investigation were either compact, or in the shape of foam. The compact ceramic samples were only shaped and sintered. Polyurethane foam was used as a preform for the manufacturing of the ceramic foam. Low viscous ceramic slurry was infiltrated into a polyurethane preform. The excessive slurry was squeezed-out, and the coated preform was dried. Finally, it was heat-treated in order to remove the polyurethane skeleton, and to sinter the ceramic powder.

Table 2 Chemical composition of AE44 alloy determined using ICP-AES (mass fraction, %)

Al	Mn	Zn	Si	Ce	La	Nd	Pr	Mg
4.94	0.21	0.03	0.02	1.95	1.71	0.48	0.28	Bal.

Table 3 Chemical composition of ceramics determined using XRF (mass fraction, %)

SiC	Al_2O_3	SiO_2	Fe_2O_3	CaO
72.3	18.3	8.8	0.5	0.1

The composite with the ceramic foam was made in the following way. The alloy was induction-melted, heated to a casting temperature (730 °C), gravity cast into a preheated mould with a ceramic insert (600 °C), covered by insulation, and cooled in the air. For the characterization of the metal−ceramic interactions, the composite samples with the compact ceramics and ceramic foam were made by a similar procedure. The differences were in the preheating temperature of the mould containing the inserted ceramics, which was 650 °C, and that the mould was placed into a preheated furnace immediately after casting, and then held at 650 °C for 10, 20, 30, and 60 min, respectively. Thereafter, it was slowly cooled in the air. The inserted ceramics was in the form of compact ceramics and ceramic foam.

Optical microscopy (OM) work was conducted using the Olympus BX61 with the Analysis Materials Research Lab 5.0 software, and the scanning electron microscopy (SEM) work was conducted using a FEI SIRION NC. The transmission electron microscopy (TEM) observation was carried out on a Jeol JEM−2100 and a FEI Tecnai F20. The TEM specimen for the Jeol JEM−2100 was prepared using the ion beam etching in a Jeol EM−09100IS ion slicer, and for the FEI Tecnai F20, specimen was cut out at specific site using the focussed ion beam (FIB) in a FEI Nova 200. The indentation hardness was determined using an Agilent Nano Indenter G200 testing machine (a Berkovich diamond indenter, depth limit of 500 nm, strain rate target of 0.05 cycle/s, harmonic displacement target of 2 nm, and a frequency target of 45 Hz). The composition of the ceramics was determined using an X-ray fluorescence (XRF) analyser Niton XL3t GOLDD+(50 kVp). The X-ray diffraction (XRD) measurement for the ceramics was carried out in a Philips 17−10 using Cu K_α radiation with a scan rate of 1.2 (°)/min, and for the alloy EA44 it was conducted in a

PANalytical B.V PW3830/40 using Cu K_α radiation with a scan rate of 0.25 (°)/min.

3 Results and discussion

3.1 Magnesium alloy

The commercial AE44 alloy had already been investigated by several researchers [32−34]. The liquidus temperature of this AE44 alloy was 617.3 °C. Three phases were identified using XRD and EDS analyses (Table 4), all already known from the previous studies: α-Mg (Mg-rich solid solution), $Al_{11}RE_3$, and Al_2RE. The $Al_{10}RE_2Mn_7$ phase was also identified using EDS, however, its volume fraction was too small to be detected using XRD. Each intermetallic compound contained all rare-earth elements; however, the content of Ce was higher than the contents of the other elements.

Table 4 Lattice parameters of identified phases in AE44 alloy (determined using XRD)

Phase	Space group	Lattice parameter/nm
α-Mg	*P*63/*mmc*	a=0.32127±0.00041 c=0.52259±0.00022
$Al_{11}RE_3$	*mmm*	a=0.43797±0.00015 b=1.30199±0.00008 c=10.1185±0.00009
Al_2RE	$Fd\bar{3}m$	a=0.80734±0.00130

3.2 Ceramic foam

Figure 1 shows the structure of the $SiC-Al_2O_3-SiO_2$ ceramic foam with the interconnected primary and mainly closed secondary porosity. The cellular-shape of the primary porosity, with a mean-cell diameter of 4.23 mm, was almost identical to the shapes and sizes of those pores in the precursory polyurethane foam. The broken cell struts revealed the empty spaces within them. It was the secondary porosity that possessed a triangular-shape. This porosity was formed during sintering when the polyurethane foam was removed from the ceramic skeleton. The mean-strut thickness was 0.55 mm. The strut walls did not have a uniform thickness. They were much thinner at the vertices of the triangle (see the site indicated by *A* in Fig. 1(b)). At some places, where the ceramic slurry failed to surround the polyurethane foam entirely, the walls of the struts were incomplete, and represented a direct link between the primary and secondary porosity (see site *B* in Fig. 1(b)). The XRD and EDS results revealed that the ceramics contained four compounds (Fig. 2(a), Table 5): α-Al_2O_3, α-SiC, β-SiC, and SiO_2. The prevailing SiC was present both as α- and β-polymorphs.

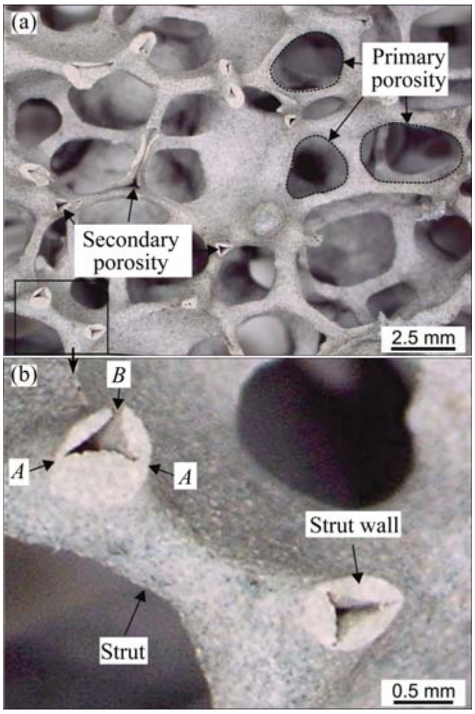

Fig. 1 Optical micrographs of ceramic foam (a) and strut (b)

3.3 Interfaces formed under different conditions

Figure 3(a) shows a part of a compact ceramic sample after 10 min exposure to the Mg-rich melt at 650 °C. These conditions were more severe than those occurring upon the manufacturing of the composite.

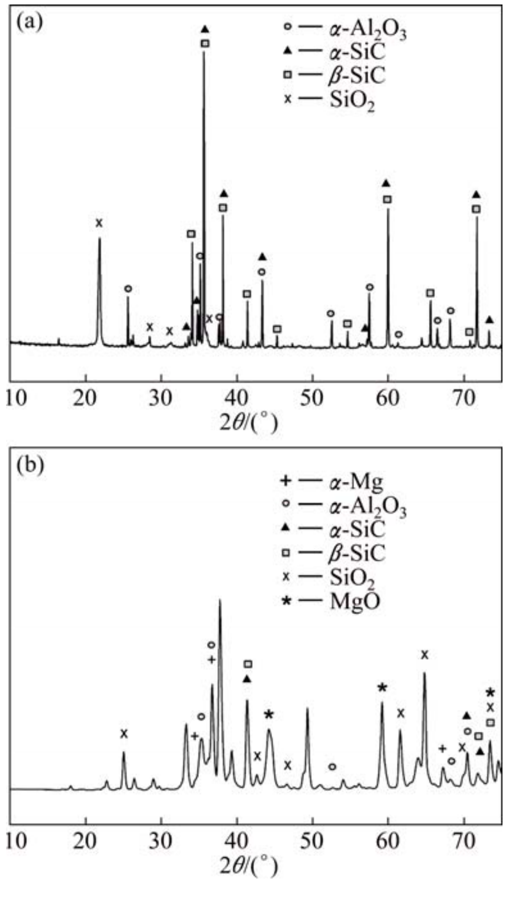

Fig. 2 XRD patterns of ceramics (a) and composite (b)

Table 5 Lattice parameters of identified compounds in ceramics determined using XRD

Phase	Space group	Lattice parameter/nm
α-Al_2O_3	$R\bar{3}c$	a=0.47646±0.00004
		c=1.30033±0.00002
α-SiC	$R3m$	a=0.30855±0.00010
		c=3.78129±0.00002
β-SiC	$P63mc$	a=0.30816±0.00011
		c=1.51182±0.00003
SiO_2	$P41212$	a=0.49870±0.00031
		c=0.69980±0.00061

Thus, they offered useful indications regarding the directions and mechanisms of those processes taking place during the contact between the ceramics and this Mg alloy. The penetration depth of the Mg-rich melt into the compact ceramic sample was not uniform. The minimum penetration depth was 0.5 mm, whilst the maximum exceeded 2 mm. In addition, the ceramic sample suffered several types of damage; the strongest attack was present at those sites where the sample probably possessed flaws (cracks, delamination). Figure 3(b) shows that the Mg-rich melt not only penetrate into the ceramic sample, but also reacted with it. The SiO_2 almost completely disappeared within the penetration layer, the fraction of Al_2O_3 slightly decreased, whilst the SiC particles remained almost intact. It could be inferred that the Mg predominantly reduced the SiO_2. As a result, several reaction products formed not only within the penetration layer, but also in the Mg-melt at the interface with the ceramic samples. EDS analyses revealed the presence of MgO, and two intermetallic compounds with the general formulae AlSiRE and AlMgSiRE. These compounds will be presented later in detail.

Figure 4(a) shows the cross-sectional microstructure through a strut in the manufactured composite. A melt of 730 °C was cast into a preform preheated to 600 °C. The melt was continuously cooled, and the preform was approximately in contact for 30 s with the Mg-rich melt. During this rather short period, the melt completely filled both the primary and secondary porosities. The secondary porosity was probably filled by a combination of melt penetration through the strut walls and the melt infiltration through the holes in the strut walls, which represented direct links between the primary and secondary porosities. Similarly as in the case of the compact samples, the struts walls were almost free of SiO_2, and thus the reaction products formed on the external surfaces and within the strut walls. In addition, the reaction products were also found within the struts, in the secondary porosity, but mainly on the internal surfaces (Fig. 4(b)). The types of products were the same as that for the compact ceramic sample.

These results suggest that during the contact of the Mg-rich melt, the reaction (Eq. (1)) took place predominantly by almost completely reducing the SiO_2.

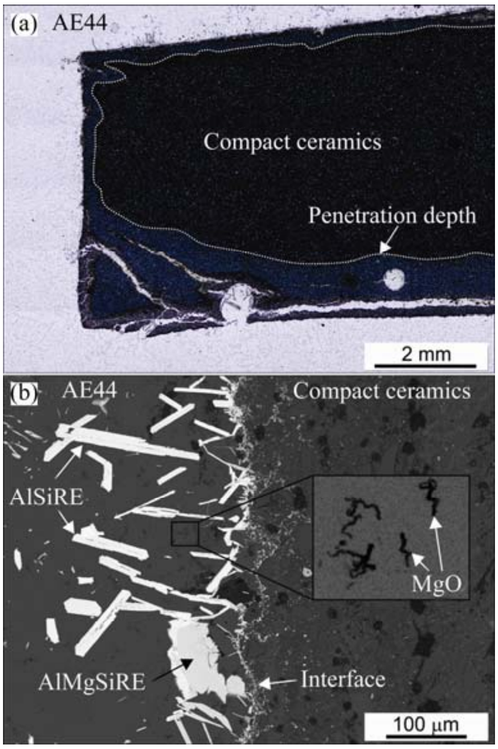

Fig. 3 Optical (a) and backscattered electron (b) micrographs of compact ceramic sample after contact with Mg-rich melt for 10 min at 650 °C

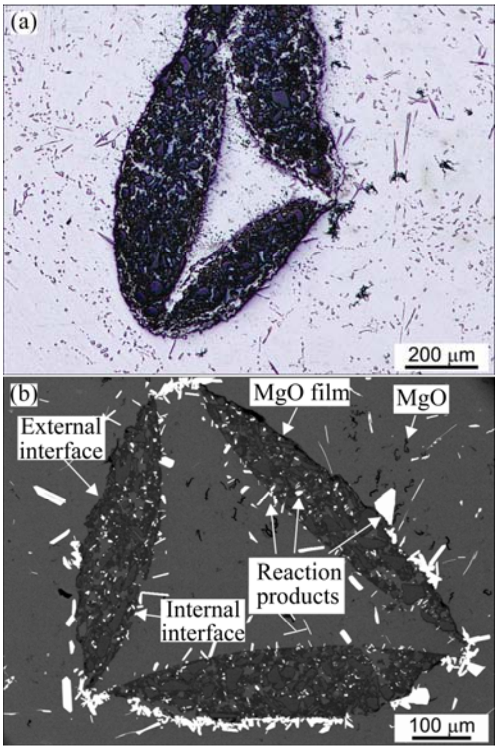

Fig. 4 Cross-sectional microstructures through strut in composite: (a) Optical micrograph; b) Backscattered electron micrograph

The reaction (Eq. (2)) also occurred, however, only to a lesser extent.

$$2Mg(l)+SiO_2(s)\rightarrow 2MgO(s)+[Si] \qquad (1)$$

$$3Mg(l)+Al_2O_3(s)\rightarrow 3MgO(s)+2[Al] \qquad (2)$$

In these reactions, l denotes the liquid phase, s denotes the solid phase, and the brackets [ ] denote the dissolved elements in the liquid phase. The main reaction product was MgO (see XRD of the composite, Fig. 2(b)). At the initial stage, it completely covered the external surfaces (Fig. 4(b)). The exothermic reactions increased the buoyancy in the melt, which caused separation of the MgO film from the external surfaces and its disintegration into smaller parts having vermicular shapes.

The TEM investigation revealed that MgO also formed on the SiC and Al_2O_3 particles inside the ceramic strut walls (Fig. 5), and it is likely that the same occurred on the sample surface. The MgO layer consisted of grains, with an average size of ~1 μm. The EDS analyses confirmed that they only contained Mg and O.

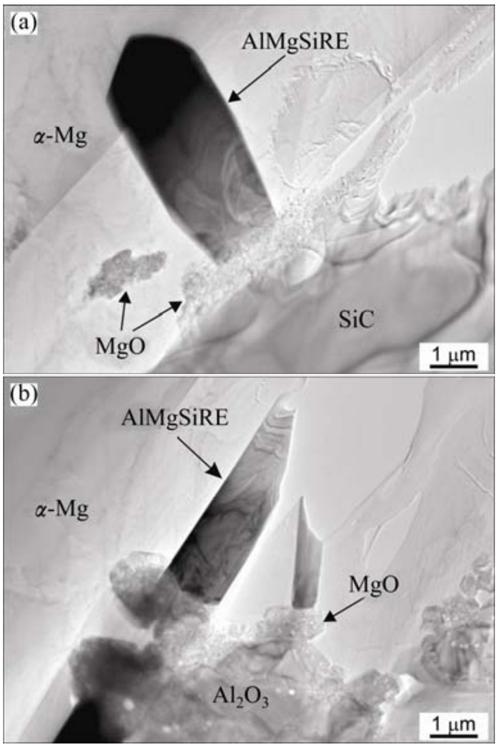

Fig. 5 Bright-field TEM micrographs of AlMgSiRE formed on MgO covered SiC (a) and Al_2O_3 (b) inside ceramic strut's wall after holding at 650 °C for 60 min

The contents of Al and Si within melt were steadily increasing whilst reactions (Eq. (1) and (Eq. (2)) took place. After exceeding the solubility products, the dissolved Al and Si reacted with the RE-elements in the melt and formed an AlSiRE-phase:

$$[Al]+[Si]+[RE]\rightarrow AlSiRE \qquad (3)$$

This phase always occurred at first. It formed on the MgO film that covered the SiC and Al_2O_3-particles (Figs. 5(a) and (b)). The AlSiRE particles later represented the nucleation sites for the AlMgSiRE phase. Thus, AlSiRE was usually partly or even completely surrounded by the AlMgSiRE, and the transformation from AlSiRE to AlMgSiRE took place with a reaction similar to a peritectic reaction (Fig. 6).

Figure 6 shows the evolution of the AlSiRE and AlMgSiRE phases. During continuous cooling, the AlMgSiRE phase prevailed, whilst only a small fraction of the AlSiRE phase remained inside the AlMgSiRE phase (Fig. 6(a)). On the other hand, during holding at 650 °C, the AlSiRE prevailed after the small reaction time (Fig. 6(b)), and afterwards mainly transformed to the AlMgSiRE phase. Only small remains of the AlSiRE phase stayed at the centres of the AlMgSiRE-particles (Figs. 6(c) and (d)).

The results of EDS analyses showed that the compositions of the AlSiRE and AlMgSiRE phases were almost the same in all the samples (Table 6). In the scientific literature, the phases with such compositions have never been reported as yet, thus they were investigated in more details.

Figures 7 and 8 show the selected area diffraction patterns of the AlSiRE and AlMgSiRE phases. The lengths of the reciprocal lattice vectors and corresponding interplanar spacing are given in Tables 7 and 8. A detailed analysis of the diffraction patterns in Fig. 7 revealed that AlSiRE possessed a tetragonal structure with the lattice parameters of a=0.62 nm and c=1.48 nm. Consequently, the diffraction patterns in Figs. 7(a)−(c) were taken along the [110], [100] and [310] zone axes of the AlSiRE, respectively. A similar analysis of Figs. 8(a)−(c) disclosed that the AlMgSiRE phase also possessed a tetragonal structure, however, with different lattice parameters: a=0.422 nm and c=1.898 nm. The diffraction patterns in Figs. 8(a)−(c) agreed with the [100], [110] and $[2\bar{1}0]$ zone axes of the AlMgSiRE, respectively.

Figure 9(a) shows a transmission electron micrograph at the interface between the AlSiRE and AlMgSiRE phases. The interface was straight, and a diffraction pattern at the interface (Fig. 9(b)) revealed specific crystallographic orientation relationships between these phases, which can be described by the following relationships: $(1\bar{1}0)_{AlSiRE}=(010)_{AlMgSiRE}$, $[110]_{AlSiRE}//[100]_{AlMgSiRE}$, and $(002)_{AlSiRE}//(002)_{AlMgSiRE}$.

Figure 10(a) shows a HRTEM-micrograph at the AlSiRE/AlMgSiRE interface. The interface was parallel to the (002) lattice planes of both phases. The periodicity wavelength was 1.520 nm in AlSiRE phase (Fig. 10(b)), and 1.887 nm in AlMgSiRE phase (Fig. 10(c)), which matched nicely with the c-parameters of both phases as

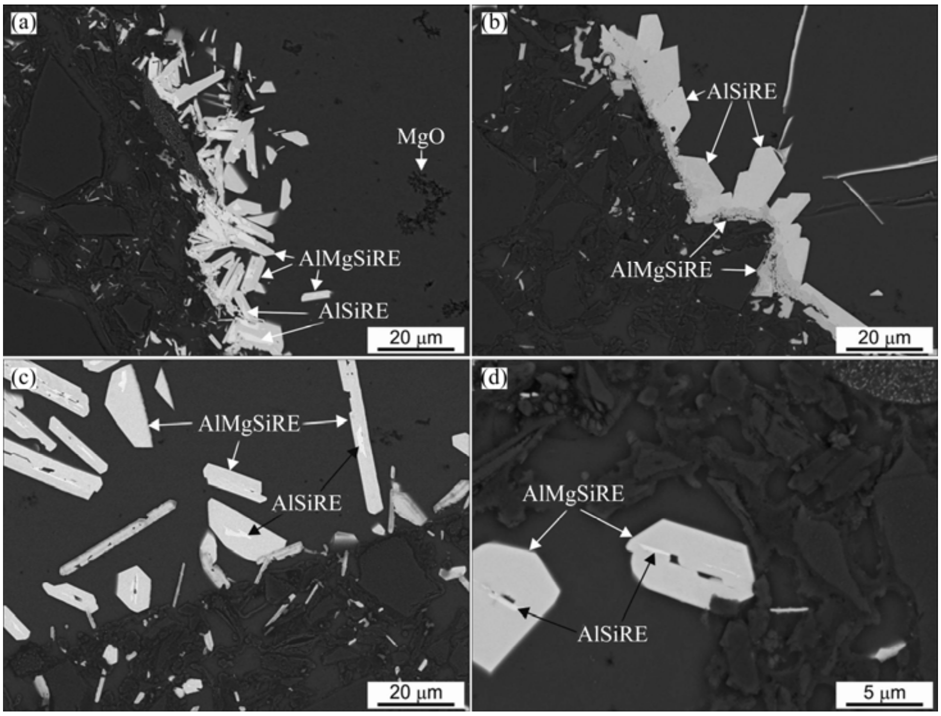

Fig. 6 Backscattered electron micrographs showing evolution of AlSiRE and AlMgSiRE phases at external interface after manufacturing (a), holding at 650 °C for 20 min (b), and holding at 650 °C for 60 min (c) and inside the ceramic strut's wall after holding at 650 °C for 60 min (d)

Table 6 Compositions of AlSiRE and AlMgSiRE reaction products under different conditions

Contact time/min	Temperature/°C	Mole fraction of AlSiRE/%			Mole fraction of AlMgSiRE/%			
		Al	Si	RE	Al	Mg	Si	RE
0.5	600	33.5	29.1	36.9	14.6	23.4	33.4	28.6
10	650	33.3	29.7	37	14.8	23.7	34.5	27
20	650	35.7	27.2	37.1	11.2	25.9	35.7	27.2
60	650	34.9	28.5	36.6	15.1	24	33.1	27.8

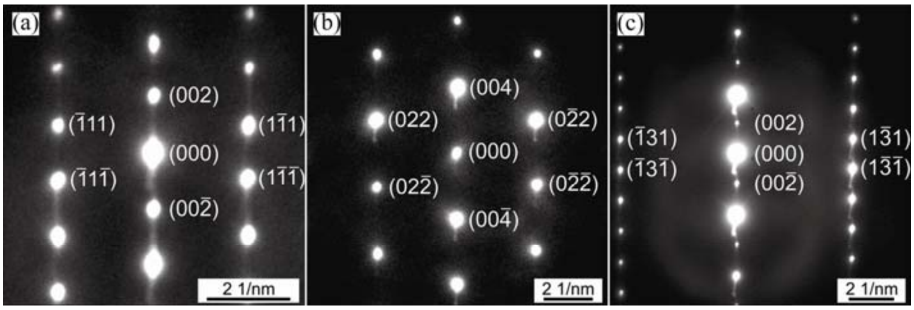

Fig. 7 Diffraction patterns of AlSiRE phase taken along [110] (a), [100] (b), and [310] (c) zone axes

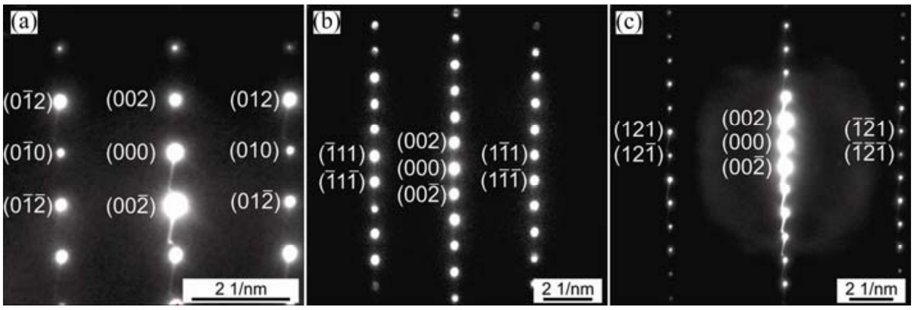

Fig. 8 Diffraction patterns of AlMgSiRE phase taken along [100] (a), [110] (b), and $[2\bar{1}0]$ (c) zone axes

Table 7 Distances between crystallographic planes in AlSiRE phase

Zone axis	Length of reciprocal lattice vectors (1/nm)			Interplanar lattice spacing/nm		
[110]	$\boldsymbol{g}_{(002)}$	$\boldsymbol{g}_{(1\bar{1}\bar{1})}$	$\boldsymbol{g}_{(1\bar{1}\bar{1})}$	$\boldsymbol{d}_{(002)}$	$\boldsymbol{d}_{(1\bar{1}\bar{1})}$	$\boldsymbol{d}_{(1\bar{1}\bar{1})}$
	1.359	2.391	2.383	0.7358	0.4182	0.4196
[100]	$\boldsymbol{g}_{(004)}$	$\boldsymbol{g}_{(0\overline{22})}$	$\boldsymbol{g}_{(0\overline{22})}$	$\boldsymbol{d}_{(004)}$	$\boldsymbol{d}_{(0\overline{22})}$	$\boldsymbol{d}_{(0\overline{22})}$
	2.72	3.534	3.549	0.3676	0.2829	0.2817
[310]	$\boldsymbol{g}_{(002)}$	$\boldsymbol{g}_{(0\bar{3}\bar{1})}$	$\boldsymbol{g}_{(0\bar{3}\bar{1})}$	$\boldsymbol{d}_{(002)}$	$\boldsymbol{d}_{(0\bar{3}\bar{1})}$	$\boldsymbol{d}_{(0\bar{3}\bar{1})}$
	1.34	5.118	5.294	0.7462	0.1953	0.1888

Table 8 Distances between crystallographic planes in AlMgSiRE phase

Zone axis	Length of reciprocal lattice vectors (1/nm)			Interplanar lattice spacing/nm		
[100]	$\boldsymbol{g}_{(002)}$	$\boldsymbol{g}_{(012)}$	$\boldsymbol{g}_{(010)}$	$\boldsymbol{d}_{(002)}$	$\boldsymbol{d}_{(012)}$	$\boldsymbol{d}_{(010)}$
	1.062	2.588	2.346	0.9416	0.3863	0.4262
[110]	$\boldsymbol{g}_{(002)}$	$\boldsymbol{g}_{(1\bar{1}\bar{1})}$	$\boldsymbol{g}_{(1\bar{1}\bar{1})}$	$\boldsymbol{d}_{(002)}$	$\boldsymbol{d}_{(1\bar{1}\bar{1})}$	$\boldsymbol{d}_{(1\bar{1}\bar{1})}$
	1.056	3.314	3.314	0.9469	0.3017	0.3017
$[2\bar{1}0]$	$\boldsymbol{g}_{(002)}$	$\boldsymbol{g}_{(\bar{1}\bar{2}\bar{1})}$	$\boldsymbol{g}_{(\bar{1}\bar{2}\bar{1})}$	$\boldsymbol{d}_{(002)}$	$\boldsymbol{d}_{(\bar{1}\bar{2}\bar{1})}$	$\boldsymbol{d}_{(\bar{1}\bar{2}\bar{1})}$
	1.068	5.295	5.298	0.9363	0.1888	0.1887

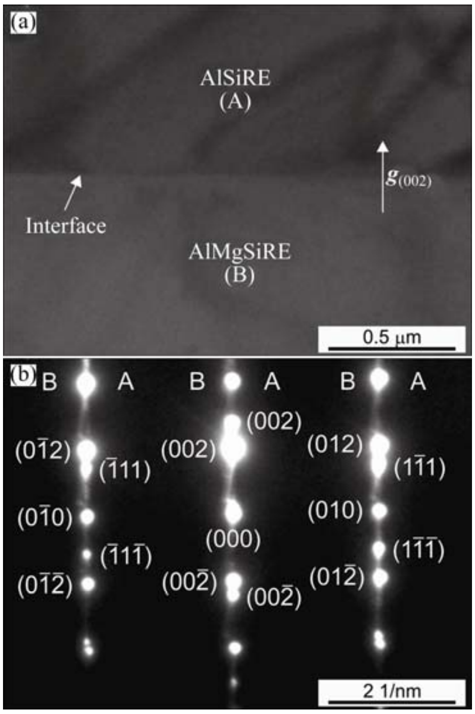

Fig. 9 AlSiRE/AlMgSiRE interface: (a) TEM micrograph; (b) Corresponding diffraction pattern (Zone axis was [110] for AlSiRE and [100] for AlMgSiRE)

determined from the SADPs: 1.48 nm for AlSiRE and 1.889 nm for AlMgSiRE. It seems that the similarity of both crystal structures allowed epitaxial growth of AlMgSiRE on AlSiRE.

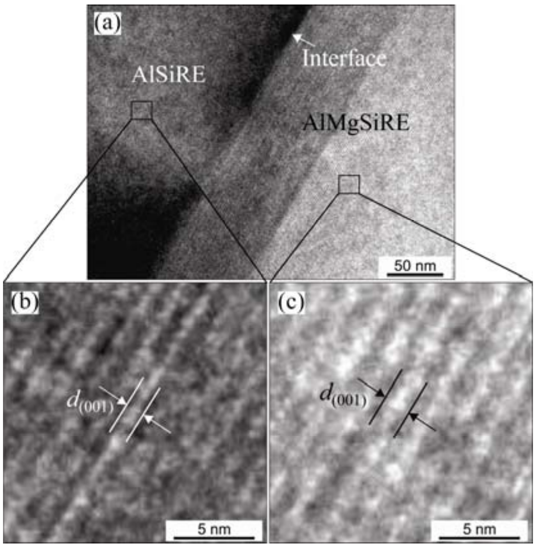

Fig. 10 HRTEM-micrographs at AlSiRE/AlMgSiRE interface: (a) Interface; (b) Enlarged image of AlSiRE; (c) Enlarged image of AlMgSiRE

In both phases, the Ce content was the greatest amongst the RE-elements. The investigations of the Al−Si−Ce ternary system revealed the presence of several ternary phases: τ_1-Ce(Si$_{1-x}$Al$_x$)$_2$, τ_2-AlCeSi$_2$, τ_3-Al$_x$CeSi$_{2-x}$, τ_4-Al$_2$CeSi$_2$, and τ_5-Al$_4$Ce$_3$Si$_6$ [35,36]. The lattice parameters of AlSiRE and AlMgSiRE disagreed with the lattice parameters of the phases in the Al−Si−Ce system, or with the lattice parameters of the other known phases formed during the interactions of Mg-alloys with ceramics. For instance, BRASZCZYNSKA et al [13,14] found Ce$_3$Si$_2$ or RE$_3$Si$_2$, and MgO at the interface between the Mg−3% RE and SiC particles (there was no Al), whereas in Ref. [20], a thick reaction layer of MgO with Al$_2$RE particles was formed at the interface between AE44 alloy and Al$_2$O$_3$ short fibres (the amount of Si was very small).

3.4 Microhardness of AlSiRE and AlMgSiRE

The measurements were carried out after reaction time of 20 and 60 min at 650 °C when the particles of both phases were large enough. The hardness of the AlSiRE was HV (1336±78), and that of AlMgSiRE was HV (917±32). Thus, both phases were very hard, yet, AlSiRE was much harder than AlMgSiRE. Thus, the formation of these phases can be attributed to the increased hardness of the composite. The effect would be stronger when AlSiRE prevailed in the microstructure.

4 Conclusions

1) The Mg-rich melt strongly reacted with the SiC−Al$_2$O$_3$−SiO$_2$ ceramics.

2) The SiO$_2$ in the ceramics was predominantly reduced.

3) The main reaction products were MgO and two novel phases AlSiRE and AlMgSiRE.

4) Both AlSiRE and AlMgSiRE possessed tetragonal structures. AlMgSiRE formed in an epitaxial way on AlSiRE, having a specific mutual orientation relationship.

5) The interaction between the Mg-rich melt and the SiC−Al_2O_3−SiO_2 ceramics was inevitable. However, by controlling the interaction time between the molten AE44 alloy and the ceramic foam, it would be possible to produce interpenetrating phase composite, having competitive properties, especially due to the very high hardnesses of the AlSiRE and the AlMgSiRE reaction products.

Acknowledgement

This work was partly financed by the Slovenian Research Agency (ARRS), projects 1000-09-310152 and L2-2269. The authors also wish to thank Mrs. Petra JUVAN, ETI, for preparing the ceramics, Mr. Tomaž MARTINČIČ, Faculty of Natural Sciences and Engineering, University of Ljubljana, for manufacturing the composite, Dr. Matej DOLENEC, Faculty of Natural Sciences and Engineering, and Dr. Ivan BRNARDIĆ, Faculty of Chemical Engineering and Technology, University of Zagreb, for the XRD analyses.

References

[1] ZESCHKY J, LO J, HÖFNER T, GREIL P. Mg alloy infiltrated Si−O−C ceramic foams [J]. Materials Science and Engineering A, 2005, 403: 215−221.

[2] CLAUSSEN N, URQUHART A W. Directed oxidation of molten metals [M]//Encyclopedia of Materials Science and Engineering. Oxford: Pergamon Press, 1990: 1111.

[3] LIU W, KÖSTER U. Criteria for formation of interpenetrating oxide/metal-composites by immersing sacrificial oxide preforms in molten metals [J]. Scripta Materialia, 1996, 35: 35−40.

[4] TOY C, SCOTT W D. Ceramic-metal composite produced by melt infiltration [J]. Journal of the American Ceramic Society, 1990, 73: 97−101.

[5] ZHANG D, SHEN P, SHI L, LIN Q, JIANG Q. Wetting and evaporation behaviors of molten Mg on partially oxidized SiC substrates [J]. Applied Surface Science, 2010, 256: 7043−7047.

[6] SHI L, SHEN P, ZHANG D, DONG E, JIANG Q. Reactive wetting in liquid magnesium/silica and magnesium/silicon systems [J]. Applied Surface Science, 2013, 274: 124−130.

[7] PRIELIPP H, KNECHTEL M, CLAUSSEN N, STREIFFER S K, MÜLLEJANS H, RÜHLE M, RÖDEL J. Strength and fracture toughness of aluminum/alumina composites with interpenetrating networks [J]. Materials Science and Engineering A, 1995, 197: 19−30.

[8] SKIRL S, HOFFMAN M, BOWMAN K, WIEDERHORN S, RÖDEL J. Thermal expansion behavior and macrostrain of Al_2O_3/Al composites with interpenetrating networks [J]. Acta Materialia, 1998, 46: 2493−2499.

[9] ZESCHKY J, GOETZ-NEUNHOEFFER F, NEUBAUER J, LO S H J, KUMMER B, SCHEFFLER M, GREIL P. Preceramic polymer derived cellular ceramics [J]. Composites Science and Technology, 2003, 63: 2361−2370.

[10] ZESCHKY J, LO S H J, SCHEFFLER M, HOEPPEL H W, ARNOLD M, GREIL P. Polysiloxane-derived ceramic foam for the reinforcement of Mg alloy [J]. Zeitschrift fur Metallkunde, 2002, 93: 812−818.

[11] KAINER K U. Basics of metal matrix composites [M]//Metal Matrix Composites, Custom-made Materials for Automotive and Aerospace Engineering. Weinheim: Wiley-VCH Verlag GmbH & Co. KGaA, 2006: 1−52.

[12] MORDIKE B L, LUKÁČ P. Interfaces in magnesium-based composites [J]. Surface and Interface Analysis, 2001, 31: 682−691.

[13] BRASZCZYŃSKA K N, LITYŃSKA L, ZYSKA A, BALIGA W. TEM analysis of the interfaces between the components in magnesium matrix composites reinforced with SiC particles [J]. Materials Chemistry and Physics, 2003, 81: 326−328.

[14] BRASZCZYŃSKA K N. Contribution of SiC particles to the formation of the structure of Mg−3wt.% RE cast composites [J]. Zeitschrift fur Metallkunde, 2003, 94: 144−148.

[15] YANG W, WEATHERLY G C, McCOMB D W, LLOYD D J. The structure of SiC-reinforced Mg casting alloys [J]. Journal of Microscopy-Oxford, 1997, 185: 292−302.

[16] HACK J E, PAGE R A, LEVERANT G R. Tensile and fatigue behavior of aluminum oxide fiber reinforced magnesium composites: Part I. Fiber fraction and orientation [J]. Metallurgical Transactions A, 1984, 15: 1389−1396.

[17] HACK J E, PAGE R A, SHERMAN R. The influence of thermal exposure on interfacial reactions and strength in aluminum oxide fiber reinforced magnesium alloy composites [J]. Metallurgical Transactions A, 1985, 16: 2069−2072.

[18] PAGE R A, HACK J E, SHERMAN R, LEVERANT G R. Tensile and fatigue behavior of aluminum oxide fiber reinforced magnesium composites: Part II. Alloying effects [J]. Metallurgical Transactions A, 1984, 15: 1397−1405.

[19] McMINN A, PAGE R A, WEI W. The effect of processing parameters on the tensile properties of alumina fiber reinforced magnesium [J]. Metallurgical Transactions A, 1987, 18: 273−281.

[20] HU B, PENG L, POWELL B R, BALOUGH M P, KUBIC R C, SACHDEV A K. Interfacial and fracture behavior of short-fibers reinforced AE44 based magnesium matrix composites [J]. Journal of Alloys and Compounds, 2010, 504: 527−534.

[21] KANEDA H, CHOH T. Fabrication of particulate reinforced magnesium composites by applying a spontaneous infiltration phenomenon [J]. Journal of Materials Science, 1997, 32: 47−56.

[22] WANG X J, HU X S, WU K, ZHENG M Y, ZHENG L, ZHAI Q J. The interfacial characteristic of SiCp/AZ91 magnesium matrix composites fabricated by stir casting [J]. Journal of Materials Science, 2009, 44: 2759−2764.

[23] LEE K B, CHOI J H, KWON H. Characteristic reaction products in the AZ91/SiC composite fabricated by pressureless infiltration technique [J]. Metals and Materials International, 2009, 15: 33−36.

[24] WU K, ZHENG M, ZHAO M, YAO C. Interfacial reaction in squeeze cast SiC_w/AZ91 magnesium alloy composite [J]. Scripta Materialia, 1996, 35: 529−534.

[25] LAN J, YANG Y, LI X C. Microstructure and microhardness of SiC nanoparticles reinforced magnesium composites fabricated by ultrasonic method [J]. Materials Science and Engineering A, 2004, 386: 284−290.

[26] YANG H R, KWON H, LEE K B. Fabrication and characterisation of AZ91/SiC composite by pressureless infiltration method [J]. Materials Science and Technology, 2011, 27: 1053−1058.

[27] REHMAN F U, FOX S, FLOWER H M, WEST D R F. Fibre/matrix interactions in magnesium-based composites containing alumina fibres [J]. Journal of Materials Science, 1994, 29: 1636−1645.

[28] SHI W, KOBASHI M, CHOH T. Effect of wettability and powder premixing on the spontaneous infiltration of molten Mg into alumina fiber preform [J]. Zeitschrift fur Metallkunde, 1999, 90: 294−298.
[29] TROJANOVÁ Z, SZÁRAZ Z, LÁBÁR J, LUKÁČ P. Deformation behaviour of an AS21 alloy reinforced by short Saffil fibres and SiC particles [J]. Journal of Materials Processing Technology, 2005, 162: 131−138.
[30] SKLENIČKA V, SVOBODA M, PAHUTOVÁ M, KUCHAŘOVÁ K, LANGDON T G. Microstructural processes in creep of an AZ91 magnesium-based composite and its matrix alloy [J]. Materials Science and Engineering A, 2001, 319: 741−745.
[31] SKLENIČKA V, PAHUTOVÁ M, KUCHAŘOVÁ K, SVOBODA M, LANGDON T G. Creep processes in magnesium alloys and their composites [J]. Metallurgical and Materials Transactions A, 2002, 33: 883−889.
[32] RZYCHOŃ T, KIEŁBUS A. Microstructure and tensile properties of sand cast and die cast AE44 magnesium alloy [J]. Archives of Metallurgy and Materials, 2008, 53: 901−907.
[33] ZHU S M, NIE J F, GIBSON M A, EASTON M A, BAKKE P. Microstructure and creep behavior of high-pressure die-cast magnesium alloy AE44 [J]. Metallurgical and Materials Transactions A, 2012, 43: 4137−4144.
[34] RZYCHOŃ T, KIEŁBUS A, CWAJNA J, MIZERA J. Microstructural stability and creep properties of die casting Mg−4Al−4RE magnesium alloy [J]. Materials Characterization, 2009, 60: 1107−1113.
[35] GRÖBNER J, MIRKOVIĆ D, SCHMID-FETZER R. Thermodynamic aspects of the constitution, grain refining, and solidification enthalpies of Al−Ce−Si alloys [J]. Metallurgical and Materials Transactions A, 2004, 35: 3349−3362.
[36] FLANDORFER H, KACZOROWSKI D, GRÖBNER J, ROGL P, WOUTERS R, GODART C. The systems Ce−Al−(Si, Ge): Phase equilibria and physical properties [J]. Journal of Solid State Chemistry, 1998, 137: 191−205.

AE44 镁合金与 $SiC-Al_2O_3-SiO_2$ 陶瓷泡沫的相互作用

Matej STEINACHER[1], Primož MRVAR[2], Franc ZUPANIČ[1]

1. Faculty of Mechanical Engineering, University of Maribor, Smetanova ulica 17, SI-2000 Maribor, Slovenia;
2. Faculty of Natural Sciences and Engineering, University of Ljubljana,
Aškerčeva cesta 12, SI-1000 Ljubljana, Slovenia

摘　要：研究熔融 AE44 镁合金与 $SiC-Al_2O_3-SiO_2$ 陶瓷之间的反应及反应产物。采用光学显微镜、电子显微镜、X 射线能量色散谱及 X 射线衍射技术对试样进行表征。在富镁熔体与陶瓷接触过程中，SiO_2 主要被 Mg 还原。MgO 为主要反应产物，而 Si 溶解在熔体中。在界面上形成两种新的四方结构相：AlSiRE 和 AlMgSiRE，这两种相具有特殊的晶体学取向关系。经短时间反应后，金属和陶瓷间可形成强连接界面，但经长时间反应后，陶瓷发生分解。

关键词：金属基复合材料；AE44 镁合金；陶瓷；界面反应

(Edited by Yun-bin HE)